

Origin of anomalous diffusion in iron mononitride thin films

Akhil Tayal,¹ Mukul Gupta,^{1,*} Ajay Gupta,² P. Rajput,³ and J. Stahn⁴

¹*UGC-DAE Consortium for Scientific Research, University Campus, Khandwa Road, Indore 452 001, India*

²*Amity Center for Spintronic Materials, Amity University, Sector 125, Noida 201 303, India*

³*Atomic & Molecular Physics Division, Bhabha Atomic Research Centre, Mumbai 400 085, India*

⁴*Laboratory for Neutron Scattering and Imaging, Paul Scherrer Institut, CH-5232 Villigen PSI, Switzerland*

(Received 24 April 2015; revised manuscript received 13 July 2015; published 24 August 2015)

In this work we aim to resolve the counterintuitive diffusion behavior of Fe and N atoms in an iron mononitride (FeN) thin film. It was observed that in spite of their larger size, Fe atoms tend to diffuse more rapidly than smaller N atoms. This only happens in the N-rich region of the Fe-N phase diagram; in N-poor regions, the N diffusion coefficient is orders of magnitude larger than that of Fe. Detailed self-diffusion measurements performed in FeN thin films reveal that the diffusion mechanism of Fe and N is different: Fe atoms diffuse through a complex process which, in addition to volume diffusion, is predominantly controlled by fast grain boundary diffusion. On the other hand, N atoms diffuse through a classical volume diffusion process. Observed results are explained in terms of stronger Fe-N (than Fe-Fe) bonds generally predicted theoretically for mononitride compositions of transition metals.

DOI: [10.1103/PhysRevB.92.054109](https://doi.org/10.1103/PhysRevB.92.054109)

PACS number(s): 66.30.Fq, 68.60.Dv, 75.50.Bb

I. INTRODUCTION

Transition metal nitrides (TMNs), especially 3d transition metal mononitrides (TMMNs), are an important class of materials exhibiting several interesting properties such as superhardness [1–4], superconductivity [5], and corrosion and wear resistance [6,7]. Among the 3d series there is a characteristic variation in the heat of formation (ΔH_f°) for the 3d TMMNs: an initial increase to a maximum is followed by a decrease and a plateau in ΔH_f° [8]. This inherently makes the formation of early 3d TMMNs, *viz.*, ScN, TiN, VN, and CrN, easier than that of late ones, *viz.*, MnN, FeN, CoN, and NiN; e.g., $\Delta H_f^\circ = -338 \text{ kJ mol}^{-1}$ for TiN [9] and -47 kJ mol^{-1} for FeN [10] at 298 K. As a result, mononitrides of Ti, V, and Cr can be easily prepared and possess excellent thermal stability, due to which they have been intensely investigated [11–15]. On the other hand, magnetic mononitrides (e.g., MnN, FeN, CoN) started to gain attention rather recently [16–23]. Unlike early 3d TMMNs, FeN or CoN can only be formed in the formation of thin films using nonequilibrium processes such as reactive sputtering [17,18,24,25], pulsed laser deposition [26], and, more recently, molecular beam epitaxy assisted with a radio-frequency-discharge nitrogen/ammonia source [21,27]. Nickel mononitrides are yet to be evidenced experimentally [28,29]. On the basis of the energetics of mononitrides, FeN and CoN are expected to be metastable.

The metastable nature of FeN turned out to be a boon, as FeN films were exploited as a source of spin injection to semiconductors or diluted magnetic semiconductors in spintronics [30]. When heated above 650 K, FeN yields a thermally stable γ' -Fe₄N, giving rise to an array of lithographically defined spin valves [30]. The mechanism leading to this structural transformation was assumed to be controlled by N diffusion. X-Ray photoelectron spectroscopy measurements for Fe 2p and N 1s peaks were used to measure N diffusion in Fe [31]. However, the conclusion

drawn from these measurements, that fast N diffusion leads to such transformations, can be misleading since interdiffusion of N in Fe, *not* self-diffusion of N, was measured. Recent Fe and N self-diffusion measurements performed using neutron reflectivity (NR) show that N self-diffusion is slower than that of Fe [18]. This is a counterintuitive result, defying established diffusion models for binary metal-metalloid systems, where a smaller atom always diffuses more rapidly than a larger atom [32]. In the absence of a suitable radioactive tracer, N self-diffusion is rather difficult to measure [13,33]. Nevertheless, by using ¹⁵N labeling, it can be obtained by doing depth-profile measurements using secondary ion mass spectroscopy (SIMS) [34,35], nuclear reaction analysis [13], and NR. Among these, the latter provides a unique opportunity to measure self-diffusion lengths down to 0.1 nm and the possibility to measure N self-diffusion in the low-temperature regime (below 500 K) [18,36].

In the present work, we have carried out a study of the Fe and N self-diffusion process to understand the origin of anomalous diffusion in nonmagnetic FeN compounds. Thin-film samples were prepared using nitrogen alone as a sputtering gas in a reactive magnetron sputtering process. X-Ray diffraction (XRD), absorption (at Fe and N K edges), and Mössbauer spectroscopy measurements confirmed the ZnS-type structure of deposited samples. NR measurements show that N diffusion is slower than Fe diffusion, however, the detailed diffusion mechanism was obtained from SIMS depth profiles using Le Claire's analysis [37,38] for grain boundary (gb) diffusion. It was found that in the low-temperature regime (up to 550 K) fast Fe diffusion takes place predominantly through the gb regions, while N diffusion is a conventional volume-type diffusion. As the temperature is increased beyond it, the difference between Fe and N diffusion decreases, leading to structural transformations—essentially triggered by Fe diffusion and followed by N diffusion to the extent that N diffuses out of the system. This is an important result defying the general misconception that fast N diffusion leads to structural instability and can be applied to understand the thermal stability of TMMNs.

*mgupta@csr.res.in; dr.mukul.gupta@gmail.com

II. EXPERIMENTAL PROCEDURE

In a direct current–magnetron sputtering technique an iron target (purity, 99.95%) was sputtered using nitrogen (purity, 99.9995%) alone as the sputtering medium at a constant power of 100 W. N₂ gas flowed at a constant rate of 10 sccm, yielding a pressure of about 0.4 Pa, while the pressure before gas flow was about 1×10^{-5} Pa. The Fe target was presputtered for 10 min using Ar gas to remove surface contaminations. The following samples were prepared at ambient temperature on Si(100) and float glass substrates.

N1: [FeN(7.9 nm)|⁵⁷FeN(7.9 nm)]_{×10}.

N2: [FeN(7.3 nm)|Fe¹⁵N(7.3 nm)]_{×10}.

S: [FeN(100 nm)|⁵⁷Fe¹⁵N(2 nm)|FeN(100 nm)].

While samples N1 and N2 were used to measure Fe and N self-diffusion using NR, respectively, sample S was used to measure Fe and N self-diffusion *simultaneously* using SIMS. Natural Fe and ⁵⁷Fe (~95% enriched) targets were sputtered using natural nitrogen and ¹⁵N (~98% enriched) gases. To avoid any mixing of nitrogen isotope gases, the chamber was evacuated after deposition of each layer and gas flows were monitored using a residual gas analyzer.

Long-range structure transformation in the samples was studied by XRD using a standard diffractometer (Bruker D8Advance) equipped with a Cu K_α x-ray source and a silicon stripe detector (Lynxeye). Microstructure of the sample was investigated using transmission electron microscopy performed on a Tecnai G²-20 transmission electron microscope operating at 200 kV. The local structure was investigated using x-ray absorption spectroscopy (XAS) and conversion electron Mössbauer spectroscopy (CEMS). The XAS measurements at the Fe K edge were performed at the BL-9 beamline [39]; those at the N K edge, at the BL-1 beamline [40], both at the Indus-2 synchrotron radiation source at Indore. While Fe K-edge measurements were carried out in fluorescence mode, those at the N K edge were measured in total electron yield mode. To study the phase transformation, samples were annealed using a vacuum furnace for about 2 h at each temperature. NR measurements were performed at the AMOR reflectometer at SINQ/PSI, Villigen, Switzerland. SIMS measurements were carried out on a Hidden Analytical SIMS Workstation using O₂⁺ as the primary source with 5 keV energy and a 400-nA beam current. The base pressure in the SIMS measurement chamber was 1×10^{-7} Pa and during measurements the pressure was of the order of 1×10^{-6} Pa due to differential pumping of the oxygen gas source.

III. RESULTS AND DISCUSSION

A. Structural measurements

Figure 1(a) shows XRD patterns of FeN thin films in the as-deposited state and after annealing at various temperatures in a vacuum furnace with a base pressure of 1×10^{-5} Pa, for 1 h at each temperature. In the as-deposited state, a single broad peak appears around $2\theta = 56^\circ$. From CEMS and XAS measurements (shown later) it was confirmed that the formed phase is γ''' -FeN having a ZnS-type structure oriented along the (220) plane [17,19]. Generally, γ''' -FeN films are oriented along the (111) direction, and the texturing along (220) observed in our samples might occur due to the

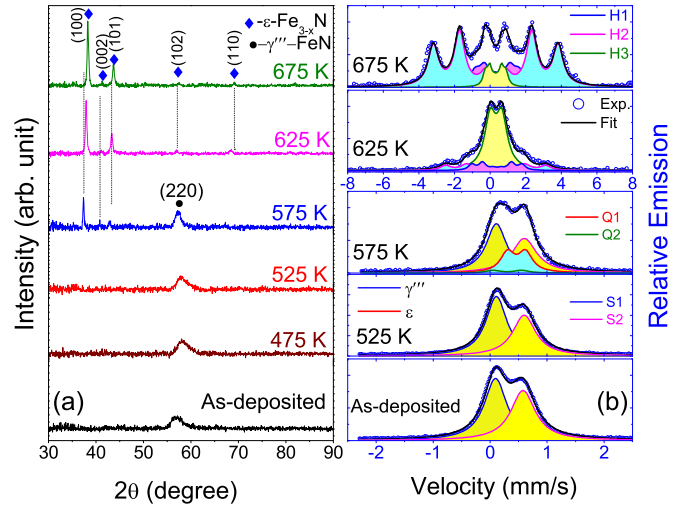


FIG. 1. (Color online) (a) XRD and (b) CEMS patterns of FeN thin films annealed at different temperatures.

somewhat different process parameters used here compared to those in earlier works [17,19]. In this work, deposition was performed at a higher flow rate of N₂ and the operating pressure was kept higher to sustain target ignition, which causes low deposition rates. This effect might have altered the film growth as observed in a similar nitride system TiN [41]. The microstructure of the as-deposited sample was also investigated using TEM, and Fig. 2 is a dark-field image showing the microstructure. TEM image clearly depicts nanocrystalline microstructure of the sample with average grain size ~5 nm.

After annealing at 475 K, a shift in the peak position towards a higher angle was observed. However, the XRD pattern of the sample annealed at 525 K is almost identical to that of the previously annealed sample. Such a shift in the peak position is an indication of annihilation of the free volume, leading to densification of the structure [42,43]. It is interesting to note that the average crystallite size (g_s) (calculated using the Scherrer formula [44]) remains at a value of about ~5 nm up to an annealing temperature of 525 K. At the higher

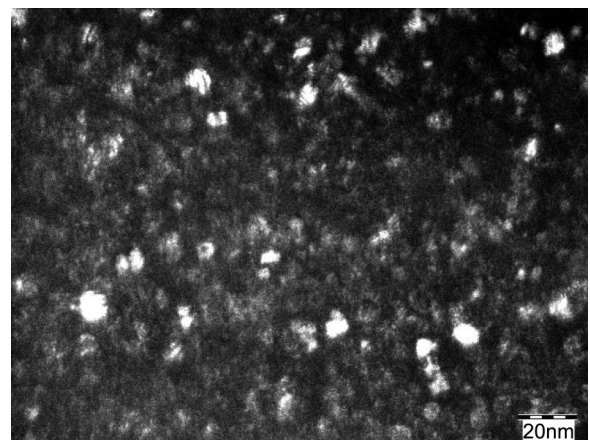


FIG. 2. TEM image showing the in-plane microstructure of an as-deposited FeN thin-film sample.

TABLE I. Conversion electron Mössbauer spectroscopy parameters for iron mononitride thin films in the as-deposited state (300 K) and after annealing at various temperatures. S, singlet; Q, doublet; H, sextet; δ , isomer shift; Γ , quadrupole splitting; **H**, hyperfine field; RA, relative area.

T (K)	Component	δ (mm/s; ± 0.03)	Γ (mm/s; ± 0.03)	H (T; ± 0.2)	RA (%; ± 2)
300	S1	0.10	–	–	54
	S2	0.57	–	–	46
525	S1	0.11	–	–	57
	S2	0.60	–	–	43
575	S1	0.11	–	–	40
	S2	0.60	–	–	34
	Q1	0.46	0.31	–	23
	Q2	0.30	0.50	–	3
625	H1	0.38	0.0	8.7	13
	H2	0.31	0.0	17.4	17
	H3	0.33	0.65	–	70
675	H1	0.40	0.0	7.6	22
	H2	0.31	0.0	21.7	68
	H3	0.30	0.0	3.6	10

temperature of 575 K, additional peaks corresponding to ε -Fe_{3-z}N ($0 \leq z \leq 1$) start to appear. With further increasing annealing temperatures, growth of the ε -Fe_{3-z}N phase can be seen. Along with it a continuous shift of peak positions towards higher 2θ values are observed, indicating that $z \rightarrow 0$.

Figure 1(b) shows CEMS spectra for FeN samples in the as-deposited state and after annealing at various temperatures. Obtained CEMS spectra were fitted using the computer program NORMOS/SITE [45] and fitted parameters are listed in Table I. The as-deposited sample and the sample annealed at 525 K show an asymmetric doublet, which is typically observed for γ' -FeN-phase crystallization in ZnS-type structures. Such spectra can be deconvoluted into two singlets: one with a smaller and the other with a larger value of the isomer shift (δ). The singlet, with $\delta = 0.01$ mm/s, corresponds to Fe surrounded tetrahedrally to N, while the other singlet originates due to defects and vacancies [17,19,46]. Annealing above 575 K results in appreciable changes in the CEMS spectrum; at this temperature it can be best fitted using a mixture of two singlets and two quadrupole split doublets, corresponding to the γ' and ε -Fe_{3-z}N phases, respectively. The obtained fitting parameters match well with the reported values [24,46]. It is known that the ε -Fe_{3-z}N phase exists over a wide composition range in which its magnetic properties also get tuned with the nitrogen concentration [47]. It was observed that, at room temperature, as $z \rightarrow 1$, the ε -Fe_{3-z}N phase becomes nonmagnetic, whereas as $z \rightarrow 0$, it becomes ferromagnetic. The appearance of a sextet confirms ferromagnetic ordering, which is also supported by XRD results indicating that $z \rightarrow 0$ in ε -Fe_{3-z}N. The obtained fitting parameters (Table I) for CEMS spectra measured above 575 K match well with the reported values [47].

To get precise information about the local structure of Fe and N, XAS measurements at the Fe and N K edges were performed and are shown in Fig. 3. A strong pre-edge peak

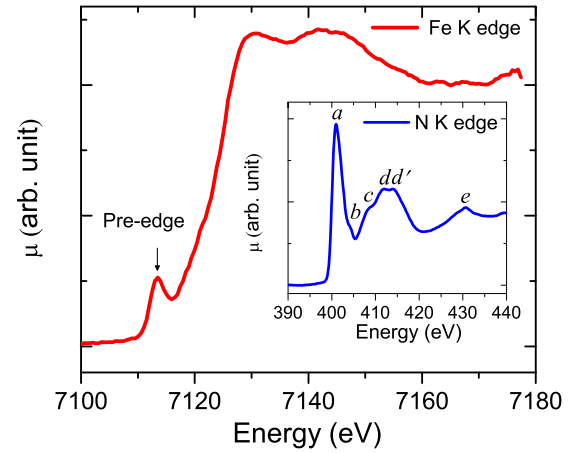


FIG. 3. (Color online) Fe K-edge XAS spectra of iron mononitride thin films. Inset: Spectra taken at the N K edge.

around 7113 eV can be seen before the Fe K edge. This is a signature of a quadrupole transition and its probability strongly depends on the direction of the local electric field, which in turns is influenced by the local site symmetry [48]. For such a pre-edge peak to appear, the inversion symmetry must be broken (transition from a bound core level to a higher level empty state). This is only possible when Fe is surrounded tetrahedrally by N atoms because this arrangement is asymmetric under inversion [48]. This clearly indicates a ZnS-type structure (tetrahedral coordination of Fe atoms) in our samples. This pre-edge feature has been frequently used to assign tetrahedral or octahedral coordination in transition metal complexes such as Mn [49] and Cr [50]. To further confirm this result, the XAS spectrum was also taken at the N K edge (shown in the inset in Fig. 3). Apart from edge feature *a* at 401 eV, three features, which are assigned as *c*, *d*, and *e*, are observed due to the electronic transition to an empty N 2*p* state hybridized to a Fe 3*d* state [19]. Various TMMNs (*viz.*, Ti, Cr, V) having a NaCl-type structure, feature *a* splits into two components due to crystal-field splitting caused by the octahedral coordination of N atoms surrounding the metal ions [51,52]. The absence of any splitting around feature *a* is a clear indication of tetrahedral coordination of Fe atoms surrounding N atoms. Less intense features (*b* and *d'*) observed in the spectra are due to the surface oxidation state [19]. Combining the information obtained from XAS measurements, it can be confirmed that the FeN phase has a ZnS-type structure. This is also in agreement with low-temperature high-field Mössbauer spectroscopy measurements in this compound [17].

B. Self-diffusion measurements

NR is a precise tool to measure atomic self-diffusion, and diffusivities as low as 1×10^{-25} m² s⁻¹ have been measured using this technique [35,36,53–55]. It is known that the neutron scattering length (b_n) varies for the isotopes ^{natural}Fe, ⁵⁷Fe, ^{natural}N, and ¹⁵N, with $b_n = 9.45, 2.3, 9.36,$ and 6.6 fm, respectively. Therefore, periodic isotope multilayers are widely used to study atomic self-diffusion using NR [18,35,36,53–55]. Figures 4(a) and 4(b) show NR patterns for samples N1

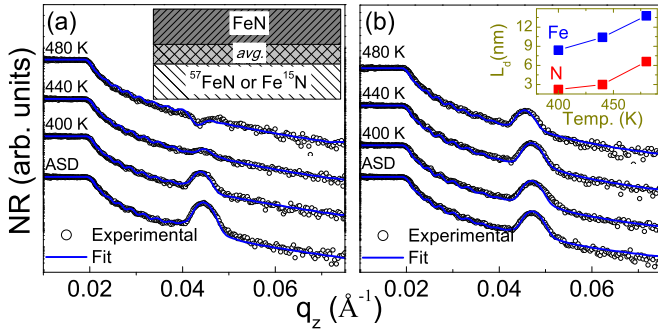


FIG. 4. (Color online) NR patterns of (a) substrate (Si)[$^{nat}\text{FeN}(7.9 \text{ nm})|^{57}\text{FeN}(7.9 \text{ nm})\times_{10}$ and (b) substrate (Si)[$|\text{Fe}^{nat}\text{N}(7.3 \text{ nm})|\text{Fe}^{15}\text{N}(7.3 \text{ nm})\times_{10}$ multilayer samples in as-deposited state and annealed at different temperatures for 2 h. Here scatter points are experimental data and the solid line is the fit to them. Inset in (b): Variation of diffusion length (L_d) obtained by fitting. Here filled and open circles represent Fe and N diffusion, respectively. Typical error bars in calculating L_d are smaller than their circles. Inset in (a): Schematic of the layer model used for fitting.

and N2, respectively. Bragg peaks appearing due to isotopic contrast of $^{nat}\text{Fe}/^{57}\text{Fe}$ and $^{nat}\text{N}/^{15}\text{N}$ can be seen clearly. Patterns were fitted using a computer program based on the Parratt formalism [56,57] and obtained layer thicknesses were 7.9 nm for sample N1 and 7.3 nm for N2. To fit NR patterns, as interdiffusion between layers takes place, a third layer is incorporated as shown schematically in the inset in Fig. 4(a). It was assumed that the b_n of this layer is the average of the two neighboring layers. As the annealing temperature increases, the thickness of this layer L_d increases, as shown in the inset in Fig. 4(b).

After annealing, the intensity of the Bragg peak starts to decay, and this decay is more rapid for sample N1 than for N2. A decay of the Bragg peak intensity is a measure of atomic diffusion across interfaces. Obtained results clearly indicate that Fe self-diffusion is faster than that of N. Detailed fitting of NR data, as discussed above, yields an L_d which is significantly larger for Fe (than N). This result, although counterintuitive, agrees well with previous studies on $\gamma''\text{-FeN}$ compounds [18]. To gain further insight leading to such anomalous behavior, we did detailed SIMS measurements on sample S. With SIMS, unlike NR, both Fe and N self-diffusion can be measured simultaneously.

Figure 5 shows the SIMS depth profiles for ^{57}Fe [Fig. 5(a)] and ^{15}N [Fig. 5(b)], isochronally annealed for 1 h at each temperature. As the annealing temperature is increased, the width of ^{57}Fe profiles becomes broader than that of ^{15}N profiles, indicating faster Fe than N self-diffusion, in agreement with NR results. Here it should be noted that the observed width of the peak associated with the ^{57}Fe and ^{15}N concentration profiles is larger by about 8–10 nm than their actual width. In addition, on the trailing side, SIMS profiles are much broader. These effects are inherently present due to the involved sputtering process in the SIMS technique, which basically causes atomic mixing and sputter roughening [58,59]. Due to atomic mixing the tracer distribution gets broader and sputter roughening causes exponential decay of the peak profile on the trailing side. Exponential decay on the trailing side of

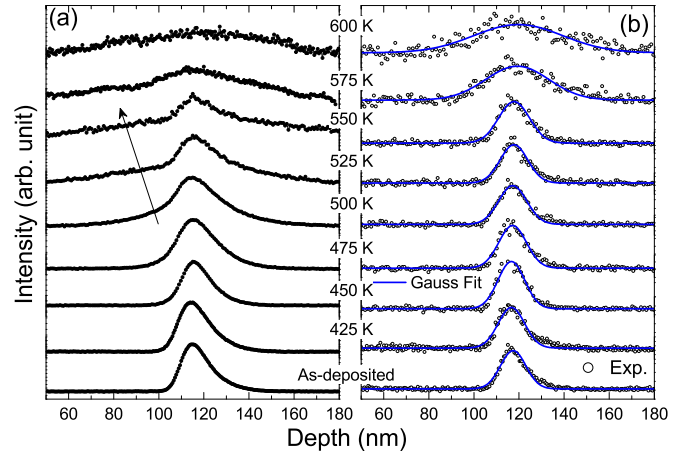


FIG. 5. (Color online) SIMS depth profile of (a) ^{57}Fe and (b) ^{15}N on a Si (substrate)[$^{nat}\text{FeN}|^{57}\text{Fe}^{15}\text{N}|^{nat}\text{FeN}$] trilayer after annealing at different temperatures.

the SIMS profile can be corrected by following specific protocols [60,61]. However, in the present work, the SIMS profile was not subject to any correction, since in this process information about gb diffusion might be affected, albeit most of the information on diffusivity can be obtained from the rising part of the SIMS profile, which always remains unaffected by any of these effects.

For such SIMS depth profiles, the concentration profile of an element at a depth z can be fitted using a Gaussian distribution function to obtain the volume diffusivity (D_V) using [61]

$$c(z,t) = \frac{\text{const.}}{\sqrt{\pi D_V t}} \exp\left(\frac{-z^2}{4D_V t}\right). \quad (1)$$

Here t is the annealing time at temperature T . Alternatively, a linear relation between $\ln(c)$ and z^2 yields the slope of the fitted line, given by slope = $-1/4D_V t$. Obtained values of N diffusivity are shown in Fig. 7(c). While ^{15}N profiles fits well to this equation, ^{57}Fe profiles cannot be fitted using Eq. (1) alone, especially above 475 K. As shown more clearly in Fig. 6, ^{15}N profiles have a single slope, and ^{57}Fe profiles have two distinct slopes. Fe diffusivity up to 475 K can be obtained using (1); above it, the additional slope can be fitted using Le Claire's analysis [37] for gb diffusion. An additional slope

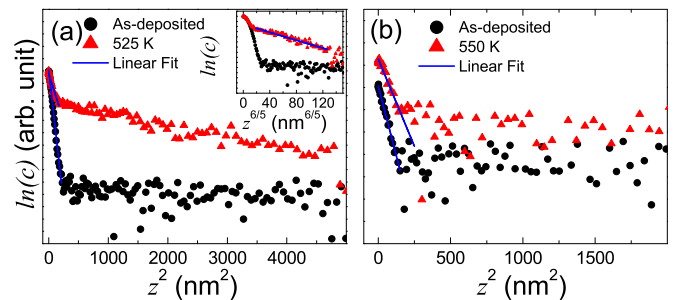


FIG. 6. (Color online) Depth profile of (a) ^{57}Fe and (b) ^{15}N plotted versus z^2 to calculate the volume diffusion, in the as-deposited and annealed state. Inset in (a): Depth profile of ^{57}Fe plotted versus $z^{6/5}$ to calculate the grain-boundary diffusion.

in ^{57}Fe depth profiles above 475 K [marked by the arrow in Fig. 5(a)] is an indication of competing diffusion processes taking place through grain boundaries in addition to a volume-type diffusion [38,62]. Since $D_{gb} \gg D_V$, it can be assumed that the fast Fe diffusion observed in our samples is primarily gb diffusion. In this case, D_{gb} can be obtained from the slope of the $\ln c$ -versus- $z^{6/5}$ curve, using Suzuoka's instantaneous source solution equation [38,63]:

$$s\delta D_{gb} = 1.084 \left(\frac{D_V^{0.91}}{t^{1.03}} \right)^{1/1.94} \left(-\frac{\partial \ln c}{\partial z^{6/5}} \right)^{-5/2.91}. \quad (2)$$

Here, s is the segregation factor, δ is the width of the gb. As such, experimental estimation of δ is difficult; a good approximation is $\delta \sim 0.5$ nm, as often reported in the literature [64]. The segregation factor s is used in this expression to accommodate the effect that arises when considering impurity diffusion. For impurity diffusion, the concentration of diffusant does not remain continuous along the grain boundaries [62]. In the present work since self-diffusion of Fe is being studied, this term can be omitted from the above expression. Equation (2) is applicable for the condition in which a dimensionless quantity, $\beta = \frac{\delta D_{gb}}{2D_V^{3/2}t^{1/2}}$, has values between 10 and 100. Since in our case we find $\beta \sim 23$ at 500 K, Eq. (2) can be applied to calculate D_{gb} . The inset in Fig. 6(a) shows a linear fit to a curve plotted between $\ln c$ and $z^{6/5}$ after annealing at 525 K. A similar analysis was carried out at other annealing temperatures and the obtained values of D_{gb} and D_V are shown figure 7(a) and 7(b), respectively.

gb diffusion is a complex process in which several elementary competing processes take place simultaneously [62]. However, for a given temperature range and duration, only a few of them may get activated. Thus different kinetic regimes of D_{gb} have been observed, ascribed by Harrison [38,65]. According to this classification, D_{gb} has three regimes known as type A, B, and C. These regimes can be differentiated according to a relation among the gb penetration depth ($L_{gb} = \sqrt{(D_{gb}t)}$), volume penetration depth ($L_V = \sqrt{(D_V t)}$), and grain size (g_s) [66]. For a type C regime $L_{gb} < g_s$, for a type B regime $L_V < g_s$, and for a type A regime $L_V > g_s$ [66]. Using these inequalities, the obtained values D_V and D_{gb} can be divided into distinct kinetic regimes as shown in Fig. 7. We find that for Fe diffusion, $L_{gb} < g_s$ ($L_{gb} \sim 2$ nm, $g_s \sim 5$ nm) for $T < 475$ K, $L_V \sim g_s$ for $475 \text{ K} < T < 550$ K, and $L_V > g_s$ for $T > 550$ K, corresponding to types C, B, and A kinetics, respectively.

On the other hand, for N diffusion, we find $L_V < g_s$ below 550 K and $L_V > g_s$ above it. This indicates that N diffusion is taking place within a grain below 550 K, and as the temperature is raised beyond it multigrain N diffusion takes over. It appears that the Fe and N diffusion mechanisms are significantly different. While only D_V takes place for N, the Fe diffusion process seems to be more complex, having distinct kinetic regimes C, B, and A as the annealing temperature increases. It is known that in the type C regime, diffusion takes place predominantly through grain boundaries, leading to segregation of Fe atoms in the gb region. This observation was also reflected in the XRD results, which show no grain growth below 525 K. It is known that grain growth occurs

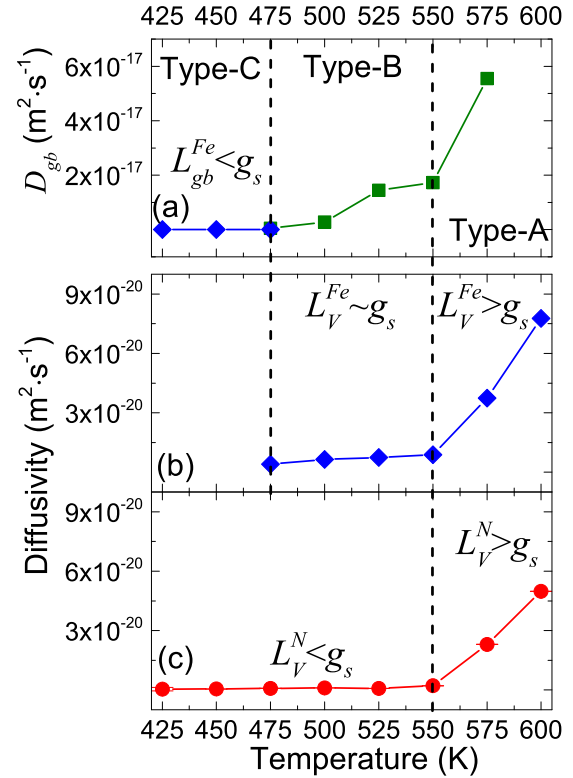


FIG. 7. (Color online) Variation of (a) D_{gb} of Fe, (b) D_V of Fe, and (c) D_V of N at different annealing temperatures. Typical error bars in the estimation of diffusivity are of the order of the size of the symbols.

with annihilation of grain boundaries which otherwise act as defects within the ordered grains. In the grain growth process, the gb energy gets minimized by reducing its volume fraction. Below 525 K, due to accumulation of Fe atoms, the gb attains thermodynamic equilibrium, which minimizes the gb energy, inhibiting grain growth [67]. In the type B regime, in addition to gb diffusion, D_V begins, though it is not effective enough to cause any structural or magnetic transformation in our case. Finally, above 550 K the D_V values of Fe and N become comparable. The observed diffusion behavior gives a direct correlation between Fe and N self-diffusion with phase transformation. This is contrary to the general preassumption that only N diffusion leads to phase transformation.

Since isochronal diffusion measurements only give a snapshot of the diffusion process, more insight into the diffusion mechanism involved was obtained by doing detailed isothermal diffusion measurements between 475 and 550 K (for Fe) and 525 and 600 K (for N) in steps of 25 K for different annealing times. Representative SIMS depth profiles taken at 525 K after various annealing times are shown in Fig. 8(a) for Fe and Fig. 8(b) for N. Following a similar process D_V and D_{gb} were calculated and are shown in Fig. 8(c). Time-dependent diffusivity data can be fitted using

$$D = D_R + A \cdot \exp(-t/\tau), \quad (3)$$

where D_R is the diffusivity in the relaxed state, A is a constant, t is the annealing time, and τ is the relaxation time. Using Eq. (3) we get $\tau = 1445 \pm 300$ and 2192 ± 300 s, respectively, for the

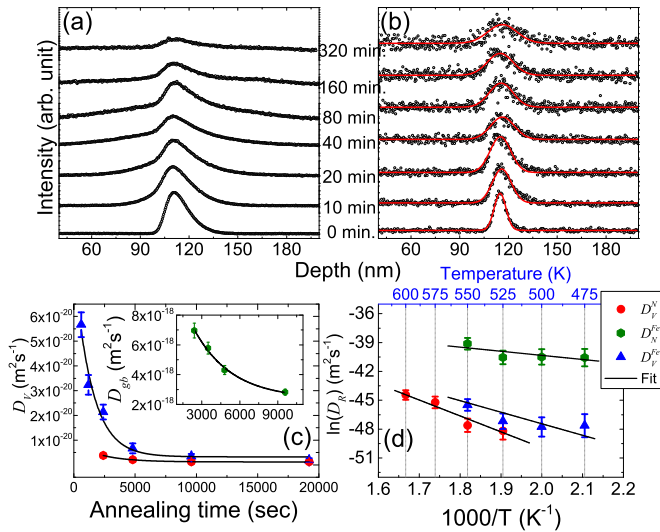


FIG. 8. (Color online) SIMS depth profile of ^{57}Fe (a) and ^{15}N (b) on Si (substrate)[$^{\text{nat}}\text{FeN}|^{57}\text{Fe}^{15}\text{N}|^{\text{nat}}\text{FeN}$] trilayer samples annealed at 525 K for different annealing times. (c) Obtained values of D_V for Fe and N annealed for different times at 525 K. Inset: Variation in the D_{gb} of Fe. (d) Arrhenius behavior of volume and grain boundary diffusion of Fe and N.

Fe and N D_V , while for the Fe D_{gb} , $\tau = 2986 \pm 300$ s. Much longer values of τ for gb diffusion indicate that it remains active for a longer time due to the availability of a large volume of gb. The obtained values of D_R follow Arrhenius behavior given by

$$D_R = D_0 \exp(-E/k_B T). \quad (4)$$

Here, D_0 denotes the pre-exponential factor, E the activation energy, T the temperature, and k_B Boltzmann's constant. The obtained values of E for the D_V of Fe and N are 1.0 ± 0.2 and 1.4 ± 0.2 eV, respectively, while for the Fe D_{gb} it is 0.6 ± 0.2 eV. As expected, the smaller value of E for gb diffusion signifies that it starts at a relatively lower temperature compared to D_V . Interestingly, we observe a slightly higher value of the activation energy for the D_V of N compared to Fe (also τ for the N D_V was larger than that for Fe).

The observed discrepancy in the D_V values of Fe and N can be understood due to the stronger metal-nitrogen (than metal-metal) interaction predicted theoretically for TMMNs [8,68]. Unlike oxides, TMNs are stabilized by dominant metal-metal interactions and therefore metal-metal bonds are stronger.

However, in mononitrides having a ZnS-type or NaCl-type structure, a volume expansion of the fcc lattice takes place to accommodate N atoms in interstitial positions. Early theoretical calculations predicted that the interaction distances are larger and the bond energies are significantly smaller for metal-metal bonds compared to metal-nitrogen bonds for $3d$ TMMNs [69]. More recent band structure calculations based on density functional theory observed localization of metal valance bonds leading to weakened metal-metal bonding in mononitrides [68]. In addition, a suppression of N migration vacancy was predicted for slightly off-stoichiometry mononitrides of various TMNs [11,12]. From these theoretical studies it can be inferred that metal-metal bonds are readily broken. This situation may lead to accumulation of Fe atoms in the gb region, leading to faster Fe compared to N diffusion, under identical thermodynamic conditions. However, more detailed experiments are required to establish the role of bond strength in dictating the self-diffusion mechanism.

IV. CONCLUSION

The iron mononitride thin films studied in this work show an anomalous self-diffusion behavior in which N atoms tend to diffuse more slowly than Fe atoms. SIMS depth-profile measurements reveal that the diffusion mechanisms for Fe and N are different. While N diffuses only via a volume-type diffusion process, Fe, in addition to volume, pre-dominantly diffuses through gb's. Fe gb diffusion was about two orders of magnitude greater than its volume diffusion. Even for volume diffusion, N diffusion was found to be less than Fe. This can be understood in terms of stronger metal-nitrogen bonds (than metal-metal bonds) predicted theoretically for TMMNs, evidenced experimentally in this work.

ACKNOWLEDGMENTS

A part of this work was performed at AMOR, Swiss Spallation Neutron Source, Paul Scherrer Institute, Villigen, Switzerland. We acknowledge D. M. Phase, D. K. Shukla, R. Sah, and S. Karwal for use of the BL1 beamline and S. N. Jha and D. Bhattacharya for the BL9 beamline. We are thankful to V. R. Reddy and A. Gome for CEMS measurements; N. P. Lalla for TEM measurements, M. Horisberger for sample preparation, and L. Behra for XRD and SIMS measurements. We are grateful to A. K. Sinha and V. Ganesan for support and encouragement. A.T. is thankful to Council of Scientific and Industrial Research (CSIR), New Delhi, India for a research fellowship.

[1] S. Vepřek, *J. Vac. Sci. Technol. A* **17**, 2401 (1999).
 [2] S.-H. Jhi, S. G. Louie, M. L. Cohen, and J. Ihm, *Phys. Rev. Lett.* **86**, 3348 (2001).
 [3] S.-H. Jhi, J. Ihm, S. G. Louie, and M. L. Cohen, *Nature* **399**, 132 (1999).
 [4] S. Hao, B. Delley, S. Vepřek, and C. Stampfl, *Phys. Rev. Lett.* **97**, 086102 (2006).
 [5] S. Yamanaka, K.-i. Hotehama, and H. Kawaji, *Nature* **392**, 580 (1998).

[6] P. Steneteg, O. Hellman, O. Y. Vekilova, N. Shulumba, F. Tasnádi, and I. A. Abrikosov, *Phys. Rev. B* **87**, 094114 (2013).
 [7] W. D. Sproul, *Science* **273**, 889 (1996).
 [8] J. Häglund, A. Fernández Guillermet, G. Grimvall, and M. Körling, *Phys. Rev. B* **48**, 11685 (1993).
 [9] M. Kopcewicz, J. Jagielski, G. Gawlik, and A. Grabias, *J. Appl. Phys.* **78**, 1312 (1995).

- [10] F. Tessier, A. Navrotsky, R. Niewa, A. Leineweber, H. Jacobs, S. Kikkawa, M. Takahashi, F. Kanamaru, and F. J. DiSalvo, *Solid State Sci.* **2**, 457 (2000).
- [11] L. Tsetseris, N. Kalfagiannis, S. Logothetidis, and S. T. Pantelides, *Phys. Rev. B* **76**, 224107 (2007).
- [12] L. Tsetseris, N. Kalfagiannis, S. Logothetidis, and S. T. Pantelides, *Phys. Rev. Lett.* **99**, 125503 (2007).
- [13] L. Hultman, *Vacuum* **57**, 1 (2000).
- [14] S. Zhang, D. Sun, Y. Fu, and H. Du, *Surf. Coat. Technol.* **167**, 113 (2003).
- [15] I. Milošev, H.-H. Strehblow, and B. Navinšek, *Thin Solid Films* **303**, 246 (1997).
- [16] A. Houari, S. F. Matar, M. A. Belkhir, and M. Nakhl, *Phys. Rev. B* **75**, 064420 (2007).
- [17] M. Gupta, A. Tayal, A. Gupta, V. Reddy, M. Horisberger, and J. Stahn, *J. Alloys Compds.* **509**, 8283 (2011).
- [18] M. Gupta, A. Tayal, A. Gupta, R. Gupta, J. Stahn, M. Horisberger, and A. Wildes, *J. Appl. Phys.* **110**, 123518 (2011).
- [19] I. Jouanny, P. Weisbecker, V. Demange, M. Grafouté, O. Peña, and E. Bauer-Grosse, *Thin Solid Films* **518**, 1883 (2010).
- [20] X. Liu, H. Lu, M. He, K. Jin, G. Yang, H. Ni, and K. Zhao, *J. Alloys Compds.* **582**, 75 (2014).
- [21] C. Navío, J. Alvarez, M. J. Capitan, F. Yndurain, and R. Miranda, *Phys. Rev. B* **78**, 155417 (2008).
- [22] X. Wang, H. Jia, W. Zheng, Y. Chen, and S. Feng, *Thin Solid Films* **517**, 4419 (2009).
- [23] S. Bhattacharyya, *J. Phys. Chem. C* **119**, 1601 (2015).
- [24] P. Schaaf, *Prog. Mater. Sci.* **47**, 1 (2002).
- [25] J.-S. Fang, L.-C. Yang, C.-S. Hsu, G.-S. Chen, Y.-W. Lin, and G.-S. Chen, *J. Vac. Sci. Technol. A* **22**, 698 (2004).
- [26] M. Gupta, A. Gupta, P. Bhattacharya, P. Misra, and L. Kukreja, *J. Alloys Compds.* **326**, 265 (2001).
- [27] M. Naito, K. Uehara, R. Takeda, Y. Taniyasu, and H. Yamamoto, *J. Cryst. Growth* **415**, 36 (2015).
- [28] D. Vempaire, F. Fettar, L. Ortega, F. Pierre, S. Miraglia, A. Sulpice, J. Pelletier, E. K. Hlil, and D. Fruchart, *J. Appl. Phys.* **106**, 073911 (2009).
- [29] H. Nishihara, K. Suzuki, R. Umetsu, T. Kanomata, T. Kaneko, M. Zhou, M. Tsujikawa, M. Shirai, T. Sakon, T. Wada, K. Terashima, and S. Imada, *Physica B (Amsterdam)* **449**, 85 (2014).
- [30] C. Navío, J. Alvarez, M. J. Capitan, J. Camarero, and R. Miranda, *Appl. Phys. Lett.* **94**, 263112 (2009).
- [31] C. Navío, M. J. Capitan, J. Álvarez, R. Miranda, and F. Yndurain, *New J. Phys.* **12**, 073004 (2010).
- [32] F. Faupel, W. Frank, M. P. Macht, H. Mehrer, K. Rätzke, H. Schober, S. K. Sharma, and H. Teichler, *Rev. Mod. Phys.* **75**, 237 (2003).
- [33] H. Matzke, *Defect and Diffusion Forum*, Vol. 83 (Trans Tech Publications, Pfaffikon, Switzerland, 1992), pp. 111–130.
- [34] H. Schmidt, G. Borchardt, M. Rudolphi, H. Baumann, and M. Bruns, *Appl. Phys. Lett.* **85**, 582 (2004).
- [35] A. Tayal, M. Gupta, N. P. Lalla, A. Gupta, M. Horisberger, J. Stahn, K. Schlage, and H.-C. Wille, *Phys. Rev. B* **90**, 144412 (2014).
- [36] H. Schmidt, M. Gupta, and M. Bruns, *Phys. Rev. Lett.* **96**, 055901 (2006).
- [37] A. D. L. Claire, *Br. J. Appl. Phys.* **14**, 351 (1963).
- [38] I. Kaur, Y. Mishin, and W. Gust, *Fundamentals of Grain and Interphase Boundary Diffusion* (Wiley, New York, 1995).
- [39] S. Basu, C. Nayak, A. K. Yadav, A. Agrawal, A. K. Poswal, D. Bhattacharyya, S. N. Jha, and N. K. Sahoo, *J. Phys. Conf. Ser.* **493**, 012032 (2014).
- [40] D. M. Phase, M. Gupta, S. Potdar, L. Behera, R. Sah, and A. Gupta, *AIP Conf. Proc.* **1591**, 685 (2014).
- [41] U. C. Oh and J. H. Je, *J. Appl. Phys.* **74**, 1692 (1993).
- [42] A. Guinier, *X-Ray Diffraction: In Crystals, Imperfect Crystals and Amorphous Bodies* (Dover, New York, 1994).
- [43] B. E. Warren, *X-Ray Diffraction* (Courier Corp., New York, 1969).
- [44] B. D. Cullity, *Elements of X-Ray Diffraction* (Addison-Wesley, Reading, MA, 1978).
- [45] R. Brand, Wissenschaftlich Elektronik GmbH, Starnberg, 1995.
- [46] D. M. Borsa and D. O. Boerma, *Hyp. Interact.* **151-152**, 31 (2003).
- [47] G. Chen, N. Jaggi, J. Butt, E. Yeh, and L. Schwartz, *J. Phys. Chem.* **87**, 5326 (1983).
- [48] G. Bunker, *Introduction to XAFS: A Practical Guide to X-ray Absorption Fine Structure Spectroscopy* (Cambridge University Press, Cambridge, UK, 2010).
- [49] T. Yamamoto, *X-Ray Spectrom.* **37**, 572 (2008).
- [50] A. Pantelouris, H. Modrow, M. Pantelouris, J. Hormes, and D. Reinen, *Chem. Phys.* **300**, 13 (2004).
- [51] C. Mitterbauer, C. Hébert, G. Kothleitner, F. Hofer, P. Schattschneider, and H. Zandbergen, *Solid State Commun.* **130**, 209 (2004).
- [52] J. Pflugger, J. Fink, G. Creelius, K. Bohnen, and H. Winter, *Solid State Commun.* **44**, 489 (1982).
- [53] M. P. Rosenblum, F. Spaepen, and D. Turnbull, *Appl. Phys. Lett.* **37**, 184 (1980).
- [54] J. Speakman, P. Rose, J. Hunt, N. Cowlam, R. E. Somekh, and A. Greer, *J. Magn. Magn. Mater.* **156**, 411 (1996).
- [55] M. Gupta, A. Gupta, J. Stahn, M. Horisberger, T. Gutberlet, and P. Allenspach, *Phys. Rev. B* **70**, 184206 (2004).
- [56] L. G. Parratt, *Phys. Rev.* **95**, 359 (1954).
- [57] C. Braun, *Parratt32—The Reflectivity Tool* (HMI, Berlin, 1997).
- [58] Y. Loirat, J. Bocquet, and Y. Limoge, *J. Non-Cryst. Solids* **265**, 252 (2000).
- [59] A. Tyagi, M.-P. Macht, and V. Naundorf, *Acta Metall. Mater.* **39**, 609 (1991).
- [60] G. Brebec, R. Seguin, C. Sella, J. Bevenot, and J. Martin, *Acta Metall.* **28**, 327 (1980).
- [61] M. Gupta, A. Gupta, S. Rajagopalan, and A. K. Tyagi, *Phys. Rev. B* **65**, 214204 (2002).
- [62] Y. Mishin and C. Herzig, *Mater. Sci. Eng. A* **260**, 55 (1999).
- [63] T. Suzuoka, *J. Phys. Soc. Jpn.* **19**, 839 (1964).
- [64] J. C. Fisher, *J. Appl. Phys.* **22**, 74 (1951).
- [65] L. G. Harrison, *Trans. Faraday Soc.* **57**, 1191 (1961).
- [66] Y. Mishin and C. Herzig, *Nanostruct. Mater.* **6**, 859 (1995).
- [67] F. Liu and R. Kirchheim, *J. Cryst. Growth* **264**, 385 (2004).
- [68] C. Paduani, *Solid State Commun.* **148**, 297 (2008).
- [69] B. Eck, R. Dronskowski, M. Takahashi, and S. Kikkawa, *J. Mater. Chem.* **9**, 1527 (1999).